SPECTRAL BANDEDNESS IN HIGH- FIDELITY COMPUTATIONAL FLUID DYNAMICS PREDICTS RUPTURE STATUS IN INTRACRANIAL ANEURYSMS*

Daniel E. MacDonald[1], Mehdi Najafi[1], Lucas Temor[1], and David A. Steinman[1]

[1]Biomedical Simulation Lab, Department of Mechanical & Industrial Engineering
University of Toronto, Toronto, Ontario, Canada

ABSTRACT

Recent studies using high-fidelity computational fluid dynamics (CFD) have revealed high-frequency flow instabilities consistent with clinical reports of bruits and "musical murmurs", which have been speculated to contribute to aneurysm growth and rupture. We hypothesized that harmonic flow instabilities ("spectral bandedness") in aneurysm CFD data may be associated with rupture status. Before testing this hypothesis, we first present a novel method for quantifying and visualizing spectral bandedness in cardiovascular CFD datasets based on musical audio-processing tools. Motivated by previous studies of aneurysm hemodynamics, we also computed a selection of existing metrics that have demonstrated association with rupture in large studies. In a dataset of 50 bifurcation aneurysm geometries modeled using high-fidelity CFD, our spectral bandedness index (SBI) was the only metric significantly associated with rupture status (AUC = 0.76, p = 0.002), with a specificity of 79% (correctly predicting 19/24 unruptured cases) and sensitivity of 65% (correctly predicting 17/26 ruptured cases). Three-dimensional flow visualizations revealed coherent regions of high SBI to be associated with strong nearwall inflow jets and vortex-shedding/flutter phenomena in the aneurysm sac. We speculate that these intracycle, coherent flow instabilities may preferentially contribute to the progressive degradation of the aneurysm wall through flow-induced vibrational mechanisms, and that their absence in high-fidelity CFD may be useful for identifying intracranial aneurysms at lower risk of rupture.

1 Introduction

An intracranial aneurysm (hereafter, simply "aneurysm") is an abnormal local outpouching of an artery in the brain and is thought to be present in about 1 in 30 adults [1, 2]. Rupture of an aneurysm is a devastating event, leading to mortality or disability in the majority of cases [1, 3]. Each aneurysm carries an annual risk of rupture of $\sim$1.4%, with a mean 5-year rupture risk of 3.4%, depending on aneurysm and patient characteristics [4]. For some aneurysms, particularly small ($<$7 mm) ones, risks associated with preventative treatment often exceed the risk of rupture, confounding the decision to treat. Clinical risk assessment scoring systems combine patient-specific (such as age, sex, history of hypertension) and aneurysm-specific (such as location and size) characteristics to stratify patients by rupture risk [4, 5]. Despite these scores, however, many aneurysms still rupture, and many are likely unnecessarily treated, indicating a pressing need for better rupture risk predictors [6].

Growth and development of IAs is thought to be driven by flow-induced progressive degradation of the wall [7]. Ultimately, rupture occurs when the stress within the wall exceeds the strength of the wall; however, patient-specific wall stresses and properties are difficult or impossible to measure noninvasively, hampering direct modeling and risk

*Citation: This article has been accepted for publication in *J Biomech Eng* 144(6), p.061004 (2022) following peer review, and the Version of Record can be accessed online at https://doi.org/10.1115/1.4053403.

assessment efforts. Instead, researchers have turned to image-based computational fluid dynamics (CFD) to investigate hemodynamic forces such as wall shear stress (WSS), as a surrogate for wall strength.

The role of WSS in the growth and rupture of IAs is complex: both high and low aneurysmal WSS have demonstrated correlation with growth and rupture, which is now thought to reflect multiple mechanobiological pathways [7]. The most recent and comprehensive case-controlled CFD study demonstrates that growth and/or rupture is associated with extreme values of WSS magnitude, concentrated and oscillatory shear stress distributions, and complex intrasaccular flow patterns [8]. Nevertheless, the underlying role of hemodynamics in aneurysm rupture is still not fully understood, and further research of aneurysm hemodynamics is required to elucidate mechanobiological pathways to rupture, and to uncover better predictors of rupture risk.

Within the past few years, high-fidelity CFD has demonstrated that many aneurysm CFD studies may be overlooking the presence of high-frequency, turbulent-like flow instabilities, owing to inadequate resolutions and/or numerics [9, 10]. Such instabilities are consistent with clinical reports and in vitro studies of bruits (sounds) emanating from the cerebrovasculature [11, 12, 13]. These high-frequency flow instabilities in high-fidelity CFD have been quantified from the perspective of energy cascades using fluctuating kinetic energy, and spectral power index (SPI), and though the prevalence of high-frequency flow instabilities may be higher than 30%, no significant association has been found with aneurysm rupture [14, 15].

Flow instabilities are often presented in publications as either pointwise measurements (velocity-time traces) or transformed to the frequency domain using full-windowed fast Fourier transforms (FFTs) [11, 16]. Pointwise measurements, however, fail to convey spatial trends and/or heterogeneities, while Fourier-transformed signals fail to represent the temporally local features of cardiovascular waveforms. Measures of spectral complexity such as SPI and proper orthogonal decomposition energy eigenspectra analysis often use full-windowed analysis on these pulsatile, unsteady datasets, which may smear out temporally local features [17, 18].

Instead, spectrograms of cardiovascular CFD data have recently been demonstrated as a method for visually summarizing spectro-temporal hemodynamic trends over a spatial domain. In Ref. [18] (and reiterated in Fig. 1(b)), spectrograms can, in some cases, reveal narrowband harmonic banding, suggesting the presence of temporally varying, intracycle periodicity in the aneurysm sac, as distinct from more broadband spectra associated with turbulent-like flow. The hemodynamic implications of such narrowband harmonic flow structures, which could preferentially trigger aneurysm wall vibrations [19], have yet to be studied in detail.

The objective of this research was to the test the hypothesis that the presence of horizontal harmonic bands in spectrograms may be associated with aneurysm rupture status. In this paper, before developing and testing this hypothesis, we first describe a novel method for quantifying the degree of bandedness observed in cardiovascular spectrograms, which draws on tools and techniques originally developed for quantifying harmonic relationships in musical audio processing applications. After testing our hypothesis, we highlight potential fluid-dynamic sources of intracycle periodicity using flow visualization.

2 Materials and Methods

2.1 Study dataset and Computational Fluid Dynamics

To compute spectral bandedness index (SBI), we used a dataset of 50 high-fidelity pulsatile CFD simulations of patient-derived bifurcation aneurysm geometries [15], taken from the open-source Aneurisk database [20]. The dataset is near-evenly split by rupture status, with 24 unruptured and 26 ruptured aneurysms, and roughly half of the CFD simulations exhibited non-negligible flow instabilities [15].

These cases were simulated using a well-validated, minimally dissipative finite element solver (Oasis [21]) with high temporal and spatial resolution, under the assumption of rigid walls and Newtonian blood rheology. Fully developed pulsatile inlet conditions were imposed using the mean velocity waveform in Fig. 1a. These were previously shown to minimize errors com- pared to patient-specific flow rates [22], which were not available in the Aneurisk database. It is important to note that the imposed inlet velocity profiles contained no instabilities, and that the (high) mesh and temporal resolutions had previously been verified as sufficient to resolve flow instabilities [9], so any instabilities that appeared arose as a result of parent artery or peri-aneurysmal geometry and flow pulsatility.

Simulations were run for three cardiac cycles of period 0.951 s using 20,000 timesteps per cycle, and only data from the third cardiac cycle was used for all analyses. Snapshots of the flow were saved every eighth time-step during the last cycle, resulting in a sampling frequency of $\sim$2629Hz and Nyquist frequency of $\sim$1314 Hz. Further simulation details, including meshing strategy, boundary conditions and solver settings, are as described in Ref. [15].

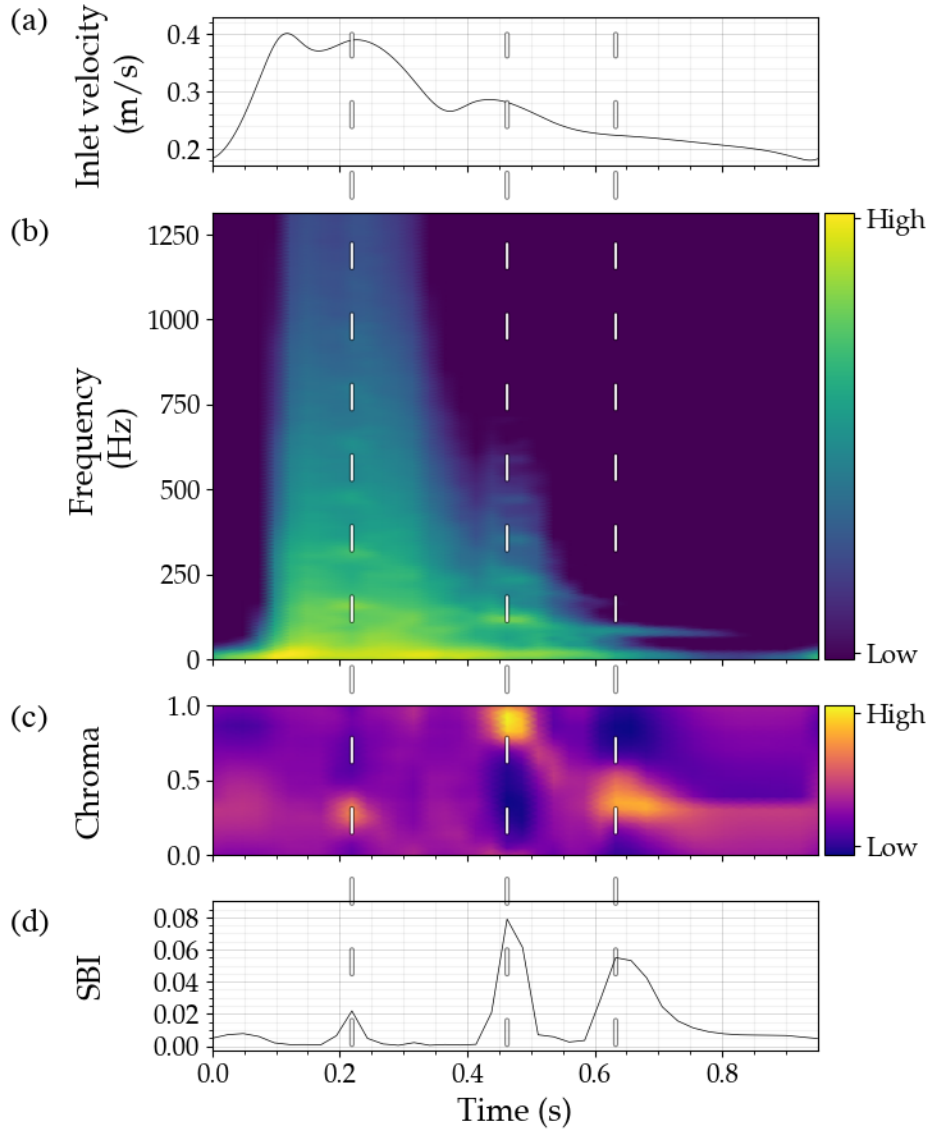

Figure 1: Calculating bandedness from spectrograms using chroma features: (a) inlet velocity waveform driving CFD simulations, (b) spectrogram derived from CFD data, (c) chromagram, and (d) bandedness.

2.2 Calculating bandedness in spectrograms

Fig. 1 demonstrates the three stages required for determining spectral bandedness: (a) calculating the spectrogram; (b) generating the chromagram; and (c) computing the bandedness as a function of time. The following subsections describe each stage in greater detail.

2.2.1 Calculating the spectrogram

Spectrograms were generated using velocity magnitude from these simulations following the method presented in [18]. As that study recommended, to balance the inherent trade-off between frequency resolution and temporal resolution, an STFT window length of 256 timesteps was chosen, and a window overlap of 75% was used resulting in a frequency resolution of 10 Hz and a time resolution of 0.024 s. Each short-time signal was windowed using a Hann window prior to FFT in order to minimize spectral leakage. A lower threshold of -20 dB was set for all spectrograms, and all analysis is based on power spectral density. Various SBI metrics were calculated from these, as detailed in the previous section. Unless otherwise indicated, the spectrograms used in this paper are sac-averaged, i.e., based on averaging spectral

data from all points within the sac (using sac delineations provided by Aneurisk [20]), and will be referred to as *sac spectrograms*. Spectrograms generated using data from a single point will be referred to as *pointwise spectrograms*.

2.2.2 Using chromagrams to capture harmonic relationships

In the sac spectrogram of Fig. 1b, horizontal bands are observed around times t=0.21, 0.45, and 0.65 s, indicating that power is concentrated at distinct frequencies. At t=0.45 s, the bands are observed to occur at near-integer multiples of some fundamental frequency. Compared with the bands at t=0.21 s, the bands at t=0.45 s demonstrate high spectral contrast relative to the underlying noise floor, suggesting that the intra-cycle periodicities are more synchronized within the sac (i.e., fluctuations of a dominant frequency occur within a larger volume of the sac). In designing the proposed spectral bandedness metric, our goal was to quantify these two qualities (harmonic power concentration and spectral contrast) of the sac spectrogram as a single scalar metric.

To measure the harmonic power concentration, we turn to musical audio-processing tools and in particular chroma features, which are a common and robust approach used for identifying harmony and melody in music. Chroma features are a cyclical representation of frequency used for identifying similar pitches across octaves of an equal-tempered scale [23]. The consecutive doubling of a given frequency (e.g., 110, 220, 440, 880 Hz) are all considered to have the same pitch class (i.e., same musical note regardless of octave) and thus chroma value, c (0.78), as given by:

$$c = \log_2 f - \lfloor \log_2 f \rfloor \tag{1}$$

where f is the frequency and $\lfloor \cdot \rfloor$ indicates the floor function. Each frequency has a unique chroma value $0 < c < 1$. The particular value of c carries no significant meaning or unit of measurement and is used only as a category to identify pitch relationships.

Each column of the spectrogram in Fig. 1b is a frequency power spectrum, whereas each column the chromagram (Fig. 1c) shows the corresponding chroma power spectrum. A chroma power spectrum can be generated from a frequency power spectrum by integrating over the power associated with each pitch class. For example, for a frequency power spectrum containing power only at 110, 220, 440, and 880 Hz, the chroma power spectrum would contain power only at c=0.78; a tone at 330 Hz would contribute additional power at c=0.37. If a given frequency power spectrum showed no distinct peaks, we would expect the chroma power spectrum to be generally flat. If power is concentrated in narrowband harmonics (as observed around 0.21, 0.45, and 0.65 s in the spectrogram of Fig. 1b), we would expect to see chroma power concentrated in a few particular chroma values (as in the chromagram of Fig. 1c). The relative flatness (vs. "peakiness") of each chroma power spectrum can thus be interpreted as a measure of spectral contrast of narrowband harmonics.

To calculate a chroma power spectrum from a frequency power spectrum, FFT bins are projected onto chroma bins using a chroma filter bank (a linear transformation matrix), where the number of discrete chroma bins N_c must be specified. In an equal-tempered musical scale, $N_c = 12$; here, outside of the conventions of Western music, we use $N_c = 24$ for increased resolution. The Python library Librosa [24] was used for constructing the chroma filter bank.

Just as a spectrogram depicts spectral power as a function of time, a chromagram depicts the chroma power over time. Regions of high intensity correspond to harmonic bands in the corresponding spectrograms, capturing power associated with harmonic structure. Where a column is relatively "flat", spectral power is distributed broadly across a range of frequencies.

2.2.3 Entropy of chroma power spectrum as a spectral bandedness index

The chromagram condenses spectral power of the spectrogram into a finite number of classes based on harmonic relationships. We then use information entropy (IE) to quantify the "flatness" of each column in the chromagram. High IE is measured for chroma spectra with high stochasticity (e.g., white noise) and low IE is measured for simple tonal signals (e.g., a sine wave). Then, by normalizing IE by the information-theoretic maximum number of bits contained in a given discrete distribution, IE is constrained to the range $[0, 1]$. To construct a spectral bandedness index (SBI) that varies from 0 (low) to 1 (high), we subtract the normalized entropy of each column of the chromagram from 1, such that 0 implies flat and 1 implies tonal:

$$\text{SBI} = 1 - \frac{-\sum_{c=1}^{N_c} x_c \log x_c}{\log N_c} \tag{2}$$

where x_c is the chroma power in bin c normalized such that $\sum_{c=1}^{N_c} x_c = 1$, and N_c is the number of chroma bins.

As shown in Fig. 1d, SBI increases where horizontal banding is present and has high contrast relative to the noise floor, and decreases where broad noise characteristics are observed. Three peaks are observed, with the first being lower than the latter two because, during systole, the spectral contrast between the harmonics and the underlying noise floor is relatively low compared to later in the cycle.

The method described herein details the calculation of SBI(t) from a sac spectrogram; we will refer to this time-varying metric (as in Fig. 1d) as sac SBI, and its cycle-averaged value as sac SBI_{avg}. All statistical analysis in this paper is based on sac SBI_{avg}; however, as will be discussed later, SBI can also, of course, be computed from pointwise spectrograms, which we will refer to as local or pointwise SBI. All 3D visualizations of bandedness in this paper are based on pointwise SBI.

In all of the above, SBI is based on spectrograms derived from averaging spectral velocity magnitude over all points within the sac volume. Given the possible mechanistic link between flow instabilities and wall vibration, we also computed SBI based on spectrograms derived from averaging spectral dynamic pressure over all points on the sac surface, denoted pSBI. A sac pSBI_{avg} metric was then calculated as the time-average of pSBI.

2.3 Calculation of previously-proposed metrics for comparison

This work is motivated by the need for better predictors of rupture risk, which has been the subject of numerous previous studies on proprietary cohorts. In an effort to contextualize those previous results on a new (and open) cohort, we computed existing hemodynamic metrics that have demonstrated association with growth or rupture in recent large, comprehensive studies. In [25], ruptured aneurysms were found to have lower time-averaged wall shear stress (TAWSS) and higher oscillatory shear index (OSI) (both sac-averaged) compared with unruptured aneurysms in a dataset of 204 aneurysms. In a systematic review (46 studies; 2791 aneurysms) of hemodynamic metrics for rupture assessment, low TAWSS was also found to be correlated with rupture, while the relative sac area exposed to low WSS (LSA) demonstrated the greatest association with rupture among widely used hemodynamic metrics [26]. Shear concentration index (SCI) quantifies the concentration of high wall shear stress on the sac, such as those induced by jet impingement phenomena, and has demonstrated association with aneurysm growth and rupture in a study of 784 aneurysms [8]. LSA and SCI are typically computed at each instant in time and then averaged over the cardiac cycle; the reader is referred to [27] for further details on how these metrics are calculated.

Spectral *power* index (SPI, a measure of the cumulative power associated with frequencies above those of the driving pulsatile flow waveform) was previously shown to be unassociated with rupture in the present dataset [15]. We include an analysis of SPI to compare and contextualize the quantity of flow instabilities (via SPI) vs. the quality of flow instabilities (via SBI) in these cases. SPI was calculated volumetrically based on the Fourier transform of velocity magnitude and is computed for the sac by averaging spectral data spatially as in [17].

Lastly, we include the pressure loss coefficient (PLc), a measure associated with energy expenditure over the aneurysm, which has also shown association with rupture [14, 28]. PLc is computed for each timestep, and the maximum instantaneous pressure loss was used for analysis. For clipping of near-vessel regions required for PLc, as well as reference WSS values for LSA and SCI, in-house VMTK-based Python scripts were created.

2.4 Statistical analysis

To test potential associations with rupture status, we performed univariate logistic regression for each previously established hemodynamic metrics (TAWSS, OSI, LSA, SCI, SPI, and PLc) and with sac SBI_{avg}. As these data were found not to follow a normal distribution, we computed significance tests using the two-sided Mann-Whitney U rank test and a critical value of $\alpha = 0.05$ to reject the null hypothesis of equivalent populations. Standard clinical receiver operating characteristics (ROC) analysis was performed to compare the performance of each regression model, as quantified by the area under each ROC curve (AUC). Curves were generated using bootstrapping by sampling with replacement [29] on the predicted probability estimates with 2000 iterations.

2.5 Visualization of intra-cycle periodicity

In order to identify the flow phenomena that are temporally and spatially associated with spectral bandedness, we created flow visualizations for a subset of cases. First, to concretely demonstrate the intra-cycle periodic flow phenomena, we visualized pointwise velocity traces and pointwise SBI for three ruptured cases that demonstrated high sac SBI_{avg}.

Then, to understand the relationship with bulk hemodynamic flow phenomena, we illustrated isosurface contours generated using pointwise SBI and compared with isosurface contours of velocity magnitude and sac spectrograms. We compared each of the previously-mentioned three ruptured cases with unruptured cases that were comparable in

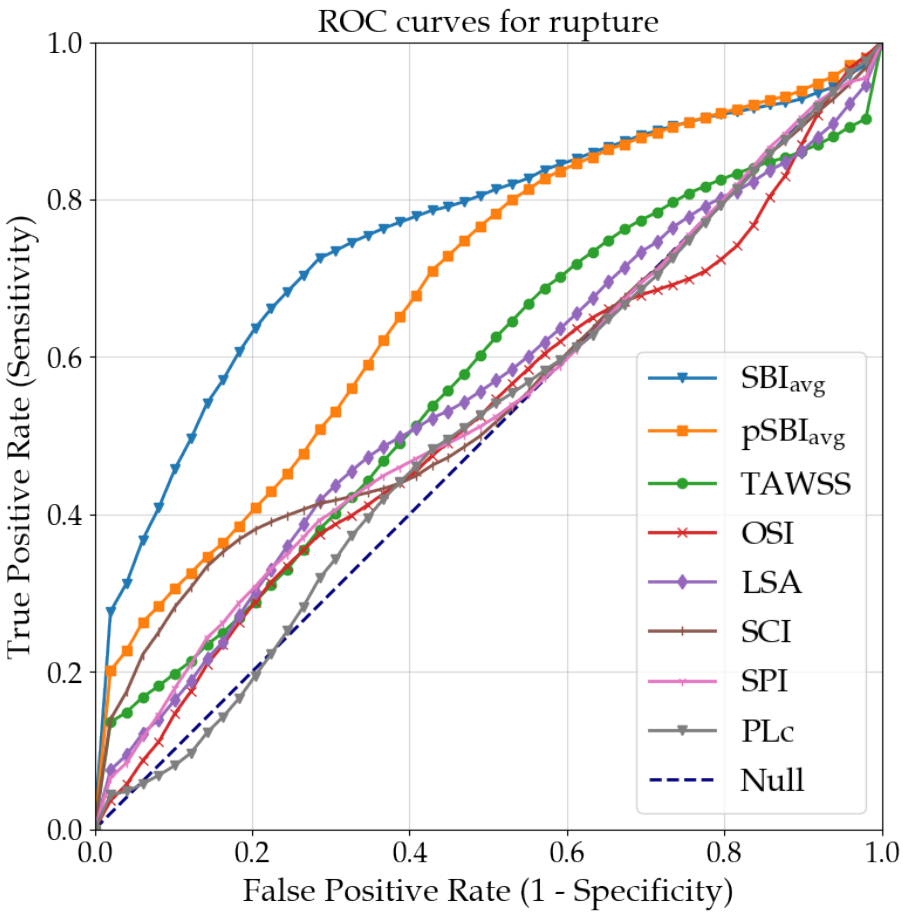

Figure 2: ROC analysis for univariate logistic regression models of sac bandedness compared with previously-established hemodynamic metrics.

terms of location, size, and SPI. Matching based on SPI ensures that pairs have a similar quantity of flow instability in order to assess and contrast the harmonic quality of these instabilities. The rupture status of each of these cases was classified correctly by the logistic regression model presented in the Results.

3 Results

3.1 Quantitative: Hypothesis testing

Table 1 summarizes the results of our hypothesis tests, while the ROC curves of Fig. 2 illustrate the performance of each classifier in this analysis. Of the computed metrics, sac SBI_{avg} was the only metric significantly associated with rupture status in the present dataset (AUC=0.76, p=0.0018). The overall accuracy of the sac SBI_{avg} model was 72%; of the cases that were truly unruptured, the model correctly classified 19/24 (specificity 79%), and of ruptured cases, 17/26 (sensitivity 65%). The wall pressure pSBI_{avg} performed more poorly, but still better than previously-proposed metrics. Compared to (velocity) SBI_{avg}, pSBI_{avg} had the same specificity, but poorer sensitivity, correctly identifying only 10/26 cases as ruptured. As summarized in Table 2, the SBI_{avg} findings were robust to variations in the spectrogram processing parameters.

3.2 Qualitative: Visualization of intra-cycle periodicity

The paired ruptured/unruptured cases referred to in this section are mapped to their Aneurisk case ID numbers in Table 3, which also includes the values used to pair them.

Table 1: Summary of hypothesis tests for univariate logistic regression models.

	AUC (95% CI)	p-value	Accuracy	Sensitivity	Specificity	R_{mean}	U_{mean}
Bandedness	0.76 (0.61-0.89)	0.0018	0.72	0.65	0.79	0.0094	0.0052
TAWSS	0.57 (0.4-0.73)	0.55	0.54	0.46	0.62	6.1	5.5
OSI	0.52 (0.36-0.69)	0.76	0.52	0.46	0.58	0.038	0.035
LSA	0.55 (0.38-0.71)	0.81	0.52	0.58	0.46	0.50	0.43
SCI	0.56 (0.39-0.72)	0.34	0.56	0.42	0.71	5.8	4.25
SPI	0.54 (0.37-0.7)	0.72	0.48	0.62	0.33	0.067	0.068
PLC	0.51 (0.35-0.67)	0.63	0.54	0.85	0.21	1.6	1.8

R_{mean} and U_{mean} denote the mean values of the ruptured and unruptured subsets, respectively.

Table 2: Sensitivity of SBI_{avg} classifier to spectrogram processing parameters.

	# files	window	AUC (95% CI)	p-value	Accuracy	Sensitivity	Specificity
Default	2500	256	0.76 (0.61-0.89)	0.0018	0.72	0.65	0.79
Fewer files	1250	128	0.77 (0.62-0.90)	0.00084	0.74	0.71	0.77
Wider window	2500	512	0.71 (0.56-0.85)	0.021	0.66	0.58	0.75
Narrower window	2500	128	0.70 (0.55-0.84)	0.024	0.66	0.62	0.71

3.2.1 Visualizing periodic instability in pointwise velocity magnitude

In Fig. 3 we show pointwise traces of velocity magnitude (u_{mag}), spectrograms, and bandedness (SBI) at the spatial location of maximum SBI for the three ruptured cases of Table 3. Note that these spectrograms are generated for a single point in the domain, and so generally have a noisier appearance compared with the sac spectrogram of Fig. 1b. Each of the u_{mag} traces are observed to oscillate periodically during some window near systole, with varying degrees of amplitude. The oscillations of case 1R are relatively low in amplitude but regular, while the traces of cases 2R and 3R are higher amplitude, higher frequency, and have higher spectral complexity. From 0.19 to 0.23 s, the fluctuations of case 3R exhibit a pattern in which every second trough dips lower than the previous; fundamentally, such a pattern would arise from the summation of two sine waves of frequencies f and 2f that are $\pi/2$ radians out of phase. This frequency relationship is apparent in the spectrogram as well, where we see two dominant bands occurring at $\sim$150 and $\sim$300 Hz.

Compared with the sac SBI_{avg} values in Table 1, the instantaneous pointwise SBI values seen in Fig. 3 demonstrate a much greater range as expected, noting the y-axis maximums of 0.1 and 0.3 respectively. In each plot of pointwise SBI, values peak with varying degrees of duration, but all are relatively brief.

3.2.2 Visualizing flow patterns associated with high spectral bandedness

Spatial locations showing high instantaneous SBI may be interpreted as regions where velocity fluctuations oscillate at some regular frequency during a narrow window in time, as determined by the spectrogram window length (here, $\sim$0.1 s). Fig. 4 shows 3D isosurface contours of u_{mag} and SBI for three pairs of cases (see Table 3) at t=0.21 s; the reader is encouraged to view the temporal animations included in the supplementary materials for viewing contours at other time points [2].

As observed in the respective sac spectrograms, each ruptured case exhibits distinct peaks in sac SBI corresponding with narrowband regions in the spectrogram. Because these are sac spectrograms, this implies that a substantial volume of the sac is experiencing spatially synchronized velocity fluctuations of a regular frequency.

The sac spectrograms of pair 1 (i.e., cases 1R and 1U) have low levels of instability as suggested by the low noise floor, with the ruptured case 1R demonstrating narrowband harmonics. Following the development of a strong jet and recirculation region in case 1R, regions of high local SBI appear within the recirculation region and surrounding the jet, as illustrated in Fig. 4. These regions of high SBI appear aligned with the direction of flow in long curling structures. Compared with case 1R, the jet of case 1U is weak, unconcentrated, and as a result quickly breaks down. Small regions of local SBI briefly appear near the neck and jet, but quickly dissipate to levels below the chosen isocontour level.

[2] Video animations are available for velocity + spectral bandedness (https://doi-org.myaccess.library.utoronto.ca/10.6084/m9.figshare.17433722.v1) and Q-criterion (https://doi-org.myaccess.library.utoronto.ca/10.6084/m9.figshare.17433968.v1)

Table 3: Descriptive characteristics of cases visualized in Figs. 4 and 5.

Pair	Location	Case name	Aneurisk case ID	Size (mm)	SPI	SBI	SBI rank (1 = highest)
1	Basilar	1R	C0068	6.0	0.0066	0.0077	13
		1U	C0054	4.8	0.022	0.0054	31
2	MCA	2R	C0050	4.1	0.16	0.0079	12
		2U	C0020	5.6	0.14	0.0035	45
3	ACA	3R	C0053	10.5	0.16	0.013	4
		3U	C0060	8.8	0.23	0.0014	50
4	MCA	4R	C0051	4.9	0.12	0.0047	37
		4U	C0099	3.4	0.0042	0.01	8

MCA = middle cerebral artery; ACA = anterior cerebral artery.
R and U denote ruptured and unruptured cases, respectively.

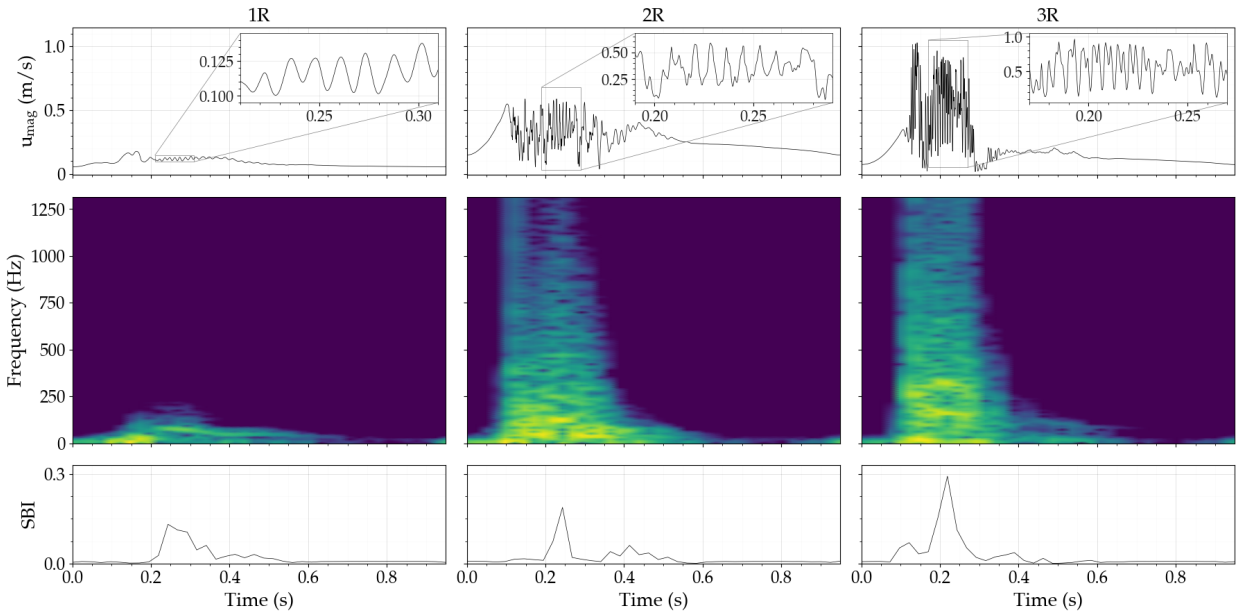

Figure 3: Visualization of pointwise instabilities at the location of maximum SBI in case 1R, case 2R, and case 3R. From top to bottom: pointwise u_{mag}; pointwise spectrograms; pointwise SBI. The inset plots in pointwise u_{mag} highlight instabilities during a period of 0.1 s where SBI is maximum.

Looking at pair 2, the sac spectrogram of the unruptured case 2U shows smooth spectral roll-off, while the ruptured case 2R shows rough bands appearing and fading through the cycle. The incoming jet of case 2R impinges near the aneurysm neck and deflects into the aneurysm cavity with a broad, spray-like structure. Sac SBI shows two periods of high activity, first near peak systole (pictured), then again near the secondary peak at t=0.4 s. During both periods, regions of high local SBI again appear as long striations aligned with bulk flow direction and colocalized with the jet. The unruptured case 2U shows a weak, unstable jet that shifts in trajectory between the aneurysm center and along the aneurysm wall. During systole, small regions of high local SBI appear and disappear sporadically, but do not persist between frames.

For pair 3, sac spectrograms for both the ruptured and unruptured cases 3R and 3U cases show a high noise floor, suggesting broad, turbulent-like instability, but only the ruptured case 3R displays narrowband harmonics. The jet of case 3R enters the sac near the wall, impinging on the dome and separating to create two large regions of recirculation. After peaking around 0.14 s, the jet destabilizes, fluctuating in trajectory throughout the systolic period. Large regions of high SBI appear as the jet begins to destabilize, again appearing as prominent, long striations surrounding the jet aligned with the direction of flow, as illustrated in Fig. 4. During diastole, the jet shifts trajectory and stabilizes, continuing to enter the sac and creating a single region of recirculation. As the jet begins to shift, bandedness breaks down momentarily before reappearing at 0.45 s and 0.60 s colocalized with the new jet location. Case 3U demonstrates a strong jet that broadens near peak-systole (pictured), splitting into two. In contrast to the ruptured case 3R, however,

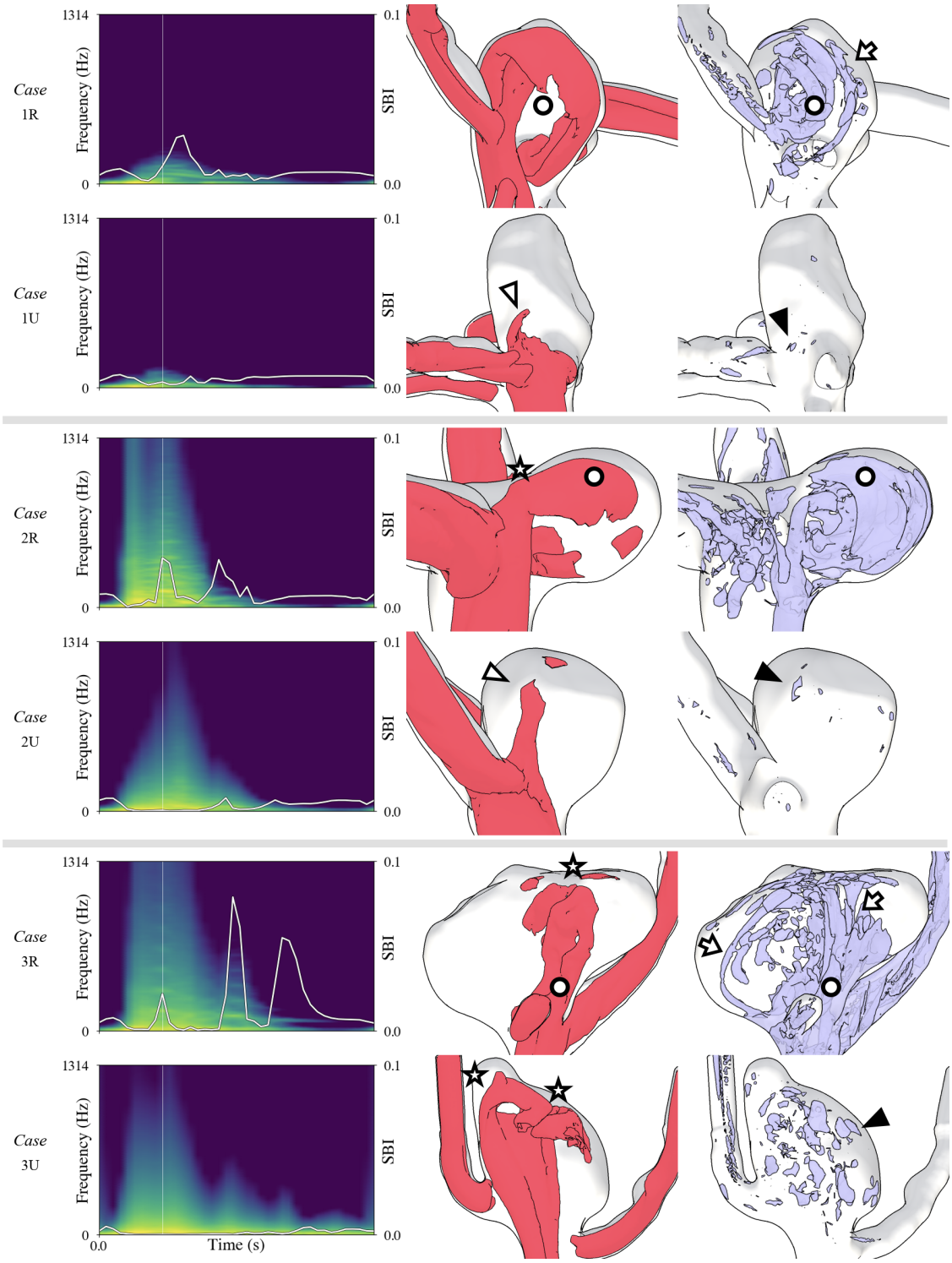

Figure 4: Contours of SBI and u_{mag} at t=0.21 s alongside the sac spectrogram for three pairs of comparable cases (see Table 3). In each pair, the top sac is ruptured and the bottom unruptured. The u_{mag} contour value for each pair is 0.5, 0.8, and 0.5 m/s; SBI contour values are 0.03, 0.06, and 0.04. The white line overlapping the spectrogram (with values indicated by the axis to the right) shows the temporal values of SBI calculated for each time window. Stars indicate impingement; arrows indicate long striations of SBI; circles indicate colocation; white triangles indicate weak jets; black triangles indicate sparse SBI.

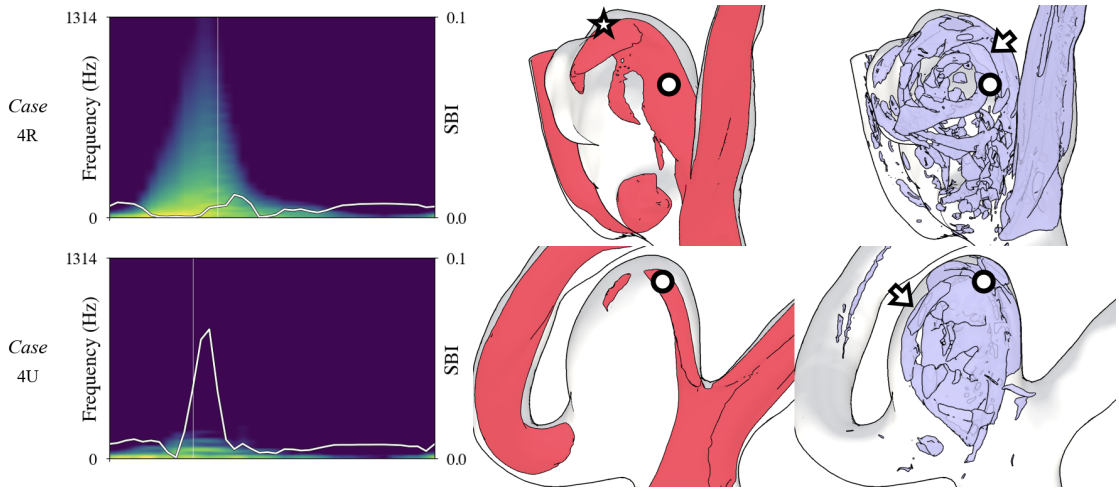

Figure 5: Contours of SBI and u_{mag} alongside sac spectrograms for two cases that were incorrectly classified by the SBI regression model. Case 4R is ruptured, case 4U is unruptured. For case 4R, the u_{mag} and SBI contour values are 0.5 m/s and 0.04. For case 4U, u_{mag} and SBI are contoured at 0.9 m/s and 0.04. Stars indicate impingement; arrows indicate long striations of SBI; circles indicate colocation.

identifying clear regions of stable recirculation in the unruptured case 3U is not straightforward given the breadth and movement of the jet. Small regions of high SBI appear throughout the cycle near the tip of the incoming jet and in the main recirculation zone, but do not persist between frames.

The above results focus on cases where the SBI logistic regression model correctly predicted rupture status. To better understand why the logistic regression did not correctly predict rupture status for some cases, in Fig. 5 we illustrate two incorrectly-classified cases: ruptured case 4R, which was incorrectly classified as unruptured; and unruptured case 4U, which was classified as ruptured. The sac spectrogram of case 4R exhibits very little in the way of narrowband harmonics, showing a high noise floor with mostly smooth roll-off. Case 4U, on the other hand, exhibits very little high-frequency spectral content, but shows distinct harmonic banding in the sub 200 Hz range.

As seen in Fig. 5, a strong, concentrated jet impinges upon the top of the dome of case 4R and deflects into the open cavity, destabilizing and generating multiple regions of recirculation. Following the destabilization of the jet, regions of high local SBI appear throughout the aneurysm, tracing out long striations in regions of recirculation. Despite these regions of high local SBI, sac SBI_{avg} is low because the sac spectrogram is smooth, implying that the harmonic content differs between different regions of the aneurysm, blurring-out spatially local spectral peaks.

Case 4U features a strong, stable, concentrated jet impinging on the aneurysm dome, generating a single recirculation zone in this relatively small aneurysm. Regions of high SBI again develop slightly after the development of a strong jet, wrapping around the jet to fill the core of the aneurysm and occupying the shear layer between the jet and the wall. Despite the incorrect prediction, the sac SBI_{avg} captures our intuitive sense of bandedness in the spectrogram, and this bandedness is additionally observed in the SBI isocontours of Fig. 5.

4 Discussion

4.1 Summary and implications of findings

Aneurysmal flow harmonics have been previously reported *in vivo*. Aaslid et al. recorded and visualized tone-like "musical murmurs" (as distinct from noise-like bruits) in the cerebral arteries of 15 patients with recent spontaneous subarachnoid hemorrhage, using transcranial Doppler ultrasound [19]. These vibrations ranged from 140 to 820 Hz and occurred as a transitional state between silent laminar flow and bruit-inducing turbulent-like flow, but the authors could only speculate that these musical murmurs were caused by periodic vortex shedding in the cerebral arteries. In the present study, we show that such tone-like fluid-dynamic instabilities exist in IAs, and that synchronized instability can dominate the sac region. These periodic instabilities are distinct from broad turbulent-like flow, and are better associated with aneurysm rupture compared with measures of broad instability such as SPI in the present dataset.

Without modelling fluid-structure interactions with patient-specific wall properties, it is of course difficult to know whether such fluid-dynamic instabilities may contribute to wall vibration, or whether the observed harmonic instabilities may be amplified or damped by a compliant wall. In an *in vitro* experiment of a patient-specific aneurysm model, Balasso et al. measured wall vibration using a laser Doppler vibrometer and investigated the effect of wall elasticity and flow rate on the spectral content of the vibrations [16]. Prominent spectral peaks occurred in the ranges 40-60 Hz and 255-265 Hz, varying slightly at the lateral wall compared to the bottom of the aneurysm. The approximate frequency of these spectral peaks was found to be largely unaffected by wall elasticity and discrete, near-doubling of flow rates, though increased elasticity did result in vibrations of greater amplitude. Further, embedding the model in fluid produced higher and smoother amplitude fluctuations compared with an open system. These findings suggest that the resonant properties determined by geometry may be an important contributor to the likelihood of flow-induced vibration compared with wall properties or flow rate. At the very least, fluid-dynamic instability is a necessary (if insufficient) condition for the development of wall vibration, and we speculate that such synchronized and periodic fluid-dynamic instabilities observed in the present study may induce resonant vibration and contribute additional stresses to and within the aneurysm wall.

If our hypothesized link between wall vibration and rupture were true, one might imagine that wall pressure instabilities would be a better predictor of rupture status than lumen velocities; however, here pSPI_{avg} performed more poorly than (velocity) SBI_{avg}. One possible explanation is that, because our models were rigid, they do not account for any fluid-structure coupling that could preferentially impact near-wall dynamic pressure instabilities, overall bulk flow dynamics within the sac are likely less susceptible to small-amplitude wall vibrations. Another possibility is that acoustic energy from intra-saccular flow instabilities propagates to the wall, even if those instabilities are damped before they reach the wall. A third possibility is that vibration alone is not the sole driver of deleterious aneurysm wall remodelling in the presence of high-frequency flow instabilities: turbulence has been shown to differentially affect endothelial cell morphology [30]; and low-frequency ($<$10 Hz) WSS harmonics have been shown to affect wall inflammation [31]. Nevertheless, it remains to be seen how or if high-frequency intermittently periodic WSS might differentially affect vascular structure or function.

As suggested by Chung et al., given the known rupture rate and population prevalence, most unruptured aneurysms are likely stable, justifying characterization between ruptured and unruptured cases [8]. Further, Chung et al. found no statistical differences between unstable and ruptured aneurysms across a wide variety of hemodynamic metrics, implying that stable unruptured aneurysms may be distinct from unstable and ruptured aneurysms. The relatively high specificity of our spectral bandedness metric suggests that the absence of harmonics may indicate aneurysm stability. Fundamentally, aneurysms without hemodynamic instabilities will not vibrate because there is no "forcing function" to excite the wall; SBI_{avg} appears to be stratifying cases based on the quality and coherence of this "forcing function", where the absence of synchronized flow phenomena indicates aneurysm stability. In a clinical setting, focusing on the identification of stable aneurysms (rather than aneurysms at high risk of rupture) may be useful for reducing the number of patients who require close monitoring.

As seen in the provided visualizations, the wide variety of aneurysm geometries makes comparing their complex flows difficult. Spectrograms, on the other hand, are an information-rich summary tool for cardiovascular CFD, communicating information about the power, duration, and quality of flow instabilities. The visual nature of spectrograms affords researchers the ability to easily compare these features and spot interesting trends between cases. If it is eventually demonstrated that high-frequency flow instabilities have predictive value for clinical decision-making, 2D spectrograms (c.f. 4D flow visualizations) may have utility for quickly and effectively interpreting CFD data in a clinical setting. Further, when applied to pointwise data as in Figs. 4 and 5, the proposed SBI introduces a new method for visualizing short-time spectral content of flow dynamics and may provide additional insight of harmonic flow structures compared with full-windowed methods such as POD.

4.2 The fluid dynamics of spectral bandedness

4.2.1 Causes of intra-cycle periodicity

As observed in Figs. 4 and 5, and the associated supplementary animations[3], regions of high SBI typically appear following the development of a strong jet in the aneurysm sac, and in regions of recirculation. Among the three cases we chose having low sac SBI_{avg}, two demonstrate weak and quickly deteriorating jets (cases 1U and 2U), while one shows a strong inflow impinging on the aneurysm dome (case 3U). The jet of that case is split, showing two points of impingement on the aneurysm sac, and appears to cause high degrees of mixing with less prominent recirculation compared to all other cases, resulting in high-frequency, turbulent-like instabilities with smooth spectral roll off.

[3] https://doi-org.myaccess.library.utoronto.ca/10.6084/m9.figshare.17433722.v1

The presence of narrowband harmonics in spectral representations of blood velocity suggests intra-cycle periodicity and has been speculated to arise from vortex-shedding phenomena (as in [18] and [19]). Vortex-shedding emerging from the aneurysm neck is readily apparent in the supplemental animation of Q-criterion of case 3R[4]. Relative to the length scales of the visualized vortex cores, the sac of this case is large and the jet is less confined, allowing the structures to traverse from the neck to the impingement zone without breaking down. In contrast, the vortex cores within the sac of cases 1R and 2R either flutter back and forth or are unable to travel due to the small sac size, repeatedly forming and breaking down. The shedding of vortex cores, the quasi-stable fluttering of vortex cores, and the periodic creation and destruction of cores appear to produce the narrowband harmonics seen in the sac spectrograms.

4.2.2 Relationship to stress concentration index (SCI)

SCI has previously demonstrated strong association with aneurysm growth and rupture in large cohort studies [8]. Being that it is a measure of jet concentration, we particularly expected SCI to be associated with the presence of turbulent-like flow instabilities resulting from high shear gradients near the jet and impingement site, and potentially with the presence of spectral bandedness. In the present dataset, the mean value of SCI was indeed higher for the ruptured cohort (5.8 vs. 4.3), but not significantly (p=0.34); Chung et al. reported a greater difference (6.2 vs. 3.8), albeit, again, with a much larger cohort [8]. Among the three pairs in Fig. 4, computed SCI was in fact always lower in the ruptured (high-bandedness) cases: 1.4 vs. 3.5, 1.8 vs. 2.2, and 2.9 vs. 6.2, respectively. On the other hand, in the mis-classified cases of Fig. 5, SCI was higher in the ruptured case. (5.9 vs. 3.2).

Of the four high sac SBI_{avg} cases of Figs. 4 and 5, three (1R, 2R, and 4U) demonstrate near-wall jets that induce a large region of recirculation throughout the cardiac cycle, while the remaining case 3R matches this description during late systole and diastole. These near-wall jets result in low values of SCI, especially in small aneurysms where the jet is confined. Though we expected SCI and SBI_{avg} to show high correlation, the presence of these near-wall jets appears to differentiate the two metrics.

Of the four low-bandedness cases, two (1U and 2U) demonstrate relatively weak jets, and two demonstrate strong jets (3U and 4R). In the cases with weak jets, only a small area extent of the sac wall exceeds the threshold to be considered high-shear stress, registering as a highly concentrated, albeit weak, impingement zone. In contrast, the jets of cases 3U and 4R induce strong, concentrated regions of high WSS near blebs.

4.2.3 Local vs. global spectral bandedness

Though SBI has theoretical bounds of 0 and 1, sac SBI values span a smaller range, peaking at only 0.04. This is to be expected given that spectral banding is often spatially localized, leading to lower spectral contrast in the sac spectrogram; and it is also temporally local, resulting in low values when averaged over time. Nevertheless, sac SBI_{avg} still has sufficient dynamic range to show a strong association with rupture in the present dataset.

In case 3R, the cycle-peak sac SBI occurs during diastole, demonstrating only a modest peak during systole. This is a consequence of the lower noise floor during diastole relative to the harmonic banding: where this spectral contrast is high, SBI is also high, and vice versa. This high spectral contrast during diastole suggests that, spatially, the harmonic content is more synchronized than during systole and occupies a larger extent of the aneurysm. The low spectral contrast during systole indicates that a broad continuum of frequencies (suggesting turbulent-like flow) is present within the large aneurysm, yet despite this, the power associated with the harmonic bands rises above the noise floor.

Conversely, in case 4R, though there are many spatial regions of high SBI, the sac spectrogram is generally smooth, suggesting that the harmonic content is not synchronized. This lack of synchronicity may be attributed to the development of multiple regions of recirculation, especially within large aneurysms of complex shape. Looking closely at the spectrogram for case 4R in Fig. 5, faint harmonic bands are nonetheless present at the instant illustrated, but the spectral contrast of these bands is low and the frequency intervals are small compared with the three ruptured cases of Fig. 4. Assessing spectral bandedness visually based on isosurface contours of SBI (as in Figs. 4 and 5) may aid in understanding the flow patterns, while assessing bandedness based on the sac spectrogram and SBI_{avg} (as in our statistical analysis) may be more appropriate for assessing global trends, especially for small aneurysms.

4.3 Limitations

4.3.1 Spectral bandedness metric

As noted in the Methods, the chroma equation maps frequencies according to a geometric progression given by the consecutive doubling of a fundamental frequency. Flow-induced harmonics are more likely to behave more closely to

[4]https://doi-org.myaccess.library.utoronto.ca/10.6084/m9.figshare.17433968.v1

integer multiples of a fundamental frequency, as suggested by the evenly spaced banding in the spectrograms of case 3R. Nevertheless, since spectral power tends to decay with frequency, we expect the chromagram to be dominated by low-frequency spectral power and, in the presence of integer harmonics, by the low-integer harmonics. Alternatively, spectral bands could be heuristically extracted from the spectrograms using image segmentation as in [32, 33], but this would rely on choosing appropriate thresholds or conditions to determine what may be considered a peak; because the spectral contrast in sac spectrograms is often low, segmentation will inevitably miss some peaks. While alternative methods may be available, the current method avoids the choice of heuristic parameters and, as demonstrated in Table 2, was robust to spectrogram processing parameters.

4.3.2 Size of dataset

The associations of other hemodynamic metrics (TAWSS, OSI, LSA, SCI, PLc) with rupture status were weaker than previously reported in [8, 25, 28]. This may well be due to our use of a smaller cohort (n=50 vs. n=784 [8], n=204 [25], n=100 [28]). On the other hand, it might be due to or our focus on bifurcation IAs compared to their cohorts of both bifurcation and sidewall IAs, since morphological and hemodynamic predictors of rupture have previously been shown to differ significantly in bifurcation vs. sidewall IAs [34]. However, our results are still in line with the association of jet impingement with rupture status [8], since jetting is typically associated with the presence of flow instabilities. Our spectral bandedness metric showed strong association with rupture status in this small dataset. This is intriguing but requires further exploration in large and/or prospective studies before it can be considered in clinical decision-making.

4.3.3 Study and modelling assumptions

As previously discussed, this analysis is based on retrospective analysis of rupture status and does not account for the relative stability of unruptured aneurysms. Like virtually all other aneurysm rupture association studies [8, 14, 25, 28], patient-specific flow rates were not available for the Aneurisk cases, so we used a well-validated power-law [22] to estimate pulsatile inflow conditions for each case. As flow instabilities are likely more sensitive to inflow rates than other hemodynamic metrics, sensitivity of bandedness to such uncertainty must still be explored and quantified [17, 35]. While it was demonstrated that the predictive value of SBI_{avg} was relatively insensitive to spectrogram processing parameters, further work is needed to understand the impact of CFD solver settings and resolutions on SBI, and more generally on the ability to resolve harmonic flow structures.

5 Conclusion

The presence, and harmonic quality, of blood flow instabilities may be an important feature in the search for predictors of intracranial aneurysm rupture. In this cohort of 50 cases, harmonic concentration of spectral power in sac spectrograms was shown to have stronger association with rupture compared to established hemodynamic predictors of rupture status. Harmonic banding in sac spectrograms is observed to result from intra-cycle, intermittent periodicity in the aneurysm sac, and thus supports further research of aneurysm wall vibration and its potential mechanobiological effects on aneurysm wall integrity.

6 Funding data

This work was supported by a grant to DAS from the Natural Sciences and Engineering Research Council (NSERC RGPIN-2018-04649). DEM was supported by an Ontario Graduate Scholarship and a Barbara & Frank Milligan Fellowship. Computations were performed on the Niagara supercomputers at the SciNet HPC Consortium, which is funded by: the Canada Foundation for Innovation; the Government of Ontario; Ontario Research Fund— Research Excellence; and the University of Toronto.

7 Nomenclature

c = chroma value
f = frequency, Hz
LSA = low-shear area
N_c = number of chroma bins
OSI = oscillatory shear index
pSBI = spectral bandedness index for wall dynamic pressure
PLc = pressure loss coefficient
SBI = spectral bandedness index for velocity magnitude
SCI = shear concentration index
SPI = spectral power index
TAWSS = time-average wall shear stress
u_{mag} = velocity magnitude, m/s
WSS = wall shear stress
x_c = chroma power in bin c

References

[1] J. L. Brisman, J. K. Song, and D. W. Newell. "Cerebral Aneurysms". In: *The New England Journal of Medicine* 355.9 (2006), pp. 928–939. DOI: 10.1056/NEJMra052760.

[2] M. H. Vlak et al. "Prevalence of unruptured intracranial aneurysms, with emphasis on sex, age, comorbidity, country, and time period: a systematic review and meta-analysis". In: *The Lancet Neurology* 10.7 (July 2011), pp. 626–636. DOI: 10.1016/S1474-4422(11)70109-0.

[3] J. I. Suarez. "Aneurysmal Subarachnoid Hemorrhage". In: *The New England Journal of Medicine* 354.4 (2006), pp. 387–96. DOI: 10.1056/NEJMra052732.

[4] J. P. Greving et al. "Development of the PHASES score for prediction of risk of rupture of intracranial aneurysms: a pooled analysis of six prospective cohort studies". In: *The Lancet Neurology* 13.1 (Jan. 2014), pp. 59–66. DOI: 10.1016/S1474-4422(13)70263-1.

[5] D. Backes et al. "Patient- and Aneurysm-Specific Risk Factors for Intracranial Aneurysm Growth: A Systematic Review and Meta-Analysis". In: *Stroke* 47.4 (Apr. 2016), pp. 951–957. DOI: 10.1161/STROKEAHA.115.012162.

[6] M. Zanaty et al. "Evidence That a Subset of Aneurysms Less Than 7 mm Warrant Treatment". In: *Journal of the American Heart Association* 5.8 (Aug. 2016), e003936. DOI: 10.1161/JAHA.116.003936.

[7] H. Meng et al. "High WSS or Low WSS? Complex Interactions of Hemodynamics with Intracranial Aneurysm Initiation, Growth, and Rupture: Toward a Unifying Hypothesis". In: *American Journal of Neuroradiology* 35.7 (July 2014), pp. 1254–1262. DOI: 10.3174/ajnr.A3558.

[8] B. Chung et al. "Identification of Hostile Hemodynamics and Geometries of Cerebral Aneurysms: A Case-Control Study". In: *American Journal of Neuroradiology* 39.10 (Oct. 2018), pp. 1860–1866. DOI: 10.3174/ajnr.A5764.

[9] M. O. Khan, K. Valen-Sendstad, and D. A. Steinman. "Narrowing the Expertise Gap for Predicting Intracranial Aneurysm Hemodynamics: Impact of Solver Numerics versus Mesh and Time-Step Resolution". In: *American Journal of Neuroradiology* 36.7 (July 2015), pp. 1310–1316. DOI: 10.3174/ajnr.A4263.

[10] K. Valen-Sendstad and D. Steinman. "Mind the Gap: Impact of Computational Fluid Dynamics Solution Strategy on Prediction of Intracranial Aneurysm Hemodynamics and Rupture Status Indicators". In: *American Journal of Neuroradiology* 35.3 (Mar. 2014), pp. 536–543. DOI: 10.3174/ajnr.A3793.

[11] K. Valen-Sendstad et al. "Direct numerical simulation of transitional flow in a patient-specific intracranial aneurysm". In: *Journal of Biomechanics* 44.16 (Nov. 2011), pp. 2826–2832. DOI: 10.1016/j.jbiomech.2011.08.015.

[12] G. G. Ferguson. "Turbulence in human intracranial saccular aneurysms". In: *Journal of Neurosurgery* 33.5 (Nov. 1970), pp. 485–497. DOI: 10.3171/jns.1970.33.5.0485.

[13] Y Kurokawa, S Abiko, and K Watanabe. "Noninvasive detection of intracranial vascular lesions by recording blood flow sounds." In: *Stroke* 25.2 (Feb. 1994), pp. 397–402. DOI: 10.1161/01.STR.25.2.397.

[14] L. Xu et al. "Flow instability detected in ruptured versus unruptured cerebral aneurysms at the internal carotid artery". In: *Journal of Biomechanics* 72 (Apr. 2018), pp. 187–199. DOI: 10.1016/j.jbiomech.2018.03.014.

[15] M. Khan et al. "On the prevalence of flow instabilities from high-fidelity computational fluid dynamics of intracranial bifurcation aneurysms". In: *Journal of Biomechanics* 127 (Oct. 2021), p. 110683. DOI: 10.1016/j.jbiomech.2021.110683.

[16] A. Balasso et al. "High-frequency wall vibrations in a cerebral patient-specific aneurysm model". In: *Biomedical Engineering / Biomedizinische Technik* 64.3 (May 2019), pp. 275–284. DOI: 10.1515/bmt-2017-0142.

[17] M. O. Khan et al. "On the quantification and visualization of transient periodic instabilities in pulsatile flows". In: *Journal of Biomechanics* 52 (Feb. 2017), pp. 179–182. DOI: 10.1016/j.jbiomech.2016.12.037.

[18] T. Natarajan et al. "On the spectrographic representation of cardiovascular flow instabilities". In: *Journal of Biomechanics* 110 (Sept. 2020), p. 109977. DOI: 10.1016/j.jbiomech.2020.109977.

[19] R. Aaslid and H. Nornes. "Musical murmurs in human cerebral arteries after subarachnoid hemorrhage". In: *Journal of Neurosurgery* 60.1 (Jan. 1984), pp. 32–36. DOI: 10.3171/jns.1984.60.1.0032.

[20] Aneurisk-Team. *AneuriskWeb*. 2012. URL: http://ecm2.mathcs.emory.edu/aneuriskweb/index (visited on 06/29/2022).

[21] M. Mortensen and K. Valen-Sendstad. "Oasis: A high-level/high-performance open source Navier–Stokes solver". In: *Computer Physics Communications* 188 (Mar. 2015), pp. 177–188. DOI: 10.1016/j.cpc.2014.10.026.

[22] C. Chnafa et al. "Errors in power-law estimations of inflow rates for intracranial aneurysm CFD". In: *Journal of Biomechanics* 80 (Oct. 2018), pp. 159–165. DOI: 10.1016/j.jbiomech.2018.09.006.

[23] M. Bartsch and G. Wakefield. "Audio thumbnailing of popular music using chroma-based representations". In: *IEEE Transactions on Multimedia* 7.1 (Feb. 2005), pp. 96–104. DOI: 10.1109/TMM.2004.840597.

[24] B. McFee et al. "librosa: Audio and Music Signal Analysis in Python". In: Austin, Texas, 2015, pp. 18–24. DOI: 10.25080/Majora-7b98e3ed-003. URL: https://conference.scipy.org/proceedings/scipy2015/brian_mcfee.html (visited on 05/24/2022).

[25] J. Xiang et al. "Hemodynamic–morphological discriminant models for intracranial aneurysm rupture remain stable with increasing sample size". In: *Journal of NeuroInterventional Surgery* 8.1 (2014), pp. 104–110. DOI: 10.1136/neurintsurg-2014-011477.

[26] L. Liang et al. "Towards the Clinical utility of CFD for assessment of intracranial aneurysm rupture – a systematic review and novel parameter-ranking tool". In: *Journal of NeuroInterventional Surgery* 11.2 (Feb. 2019), pp. 153–158. DOI: 10.1136/neurintsurg-2018-014246.

[27] F. Mut et al. "Computational hemodynamics framework for the analysis of cerebral aneurysms". In: *International Journal for Numerical Methods in Biomedical Engineering* 27.6 (June 2011), pp. 822–839. DOI: 10.1002/cnm.1424.

[28] H. Takao et al. "Hemodynamic Differences Between Unruptured and Ruptured Intracranial Aneurysms During Observation". In: *Stroke* 43.5 (May 2012), pp. 1436–1439. DOI: 10.1161/STROKEAHA.111.640995.

[29] G. L. Grunkemeier and Y. Wu. "Bootstrap resampling methods: something for nothing?" In: *The Annals of Thoracic Surgery* 77.4 (Apr. 2004), pp. 1142–1144. DOI: 10.1016/j.athoracsur.2004.01.005.

[30] P. F. Davies et al. "Turbulent fluid shear stress induces vascular endothelial cell turnover in vitro." In: *Proceedings of the National Academy of Sciences* 83.7 (Apr. 1986), pp. 2114–2117. DOI: 10.1073/pnas.83.7.2114.

[31] R. E. Feaver, B. D. Gelfand, and B. R. Blackman. "Human haemodynamic frequency harmonics regulate the inflammatory phenotype of vascular endothelial cells". In: *Nature Communications* 4.1 (June 2013), p. 1525. DOI: 10.1038/ncomms2530.

[32] X. Serra and J. Smith. "Spectral Modeling Synthesis: A Sound Analysis/Synthesis System Based on a Deterministic Plus Stochastic Decomposition". In: *Computer Music Journal* 14.4 (1990), p. 12. DOI: 10.2307/3680788.

[33] L. Temor et al. "Perceptually-Motivated Sonification of Spatiotemporally-Dynamic CFD Data". In: *Proceedings of the 26th International Conference on Auditory Display (ICAD 2021)*. Virtual Conference: International Community for Auditory Display, June 2021, pp. 202–209. DOI: 10.21785/icad2021.039. URL: http://hdl.handle.net/1853/66343 (visited on 05/24/2022).

[34] M. I. Baharoglu et al. "Identification of a dichotomy in morphological predictors of rupture status between sidewall- and bifurcation-type intracranial aneurysms: Clinical article". In: *Journal of Neurosurgery* 116.4 (Apr. 2012), pp. 871–881. DOI: 10.3171/2011.11.JNS11311.

[35] M. Najafi et al. "How patient-specific do internal carotid artery inflow rates need to be for computational fluid dynamics of cerebral aneurysms?" In: *Journal of NeuroInterventional Surgery* 13.5 (May 2021), pp. 459–464. DOI: 10.1136/neurintsurg-2020-015993.